

# Repeated large-scale retreat and advance of Totten Glacier indicated by inland bed erosion

A. R. A. Aitken<sup>1</sup>, J. L. Roberts<sup>2,3</sup>, T. D. van Ommen<sup>2,3</sup>, D. A. Young<sup>4</sup>, N. R. Golledge<sup>5,6</sup>, J. S. Greenbaum<sup>4</sup>, D. D. Blankenship<sup>4</sup> & M. J. Siegert<sup>7</sup>

**Climate variations cause ice sheets to retreat and advance, raising or lowering sea level by metres to decametres. The basic relationship is unambiguous, but the timing, magnitude and sources of sea-level change remain unclear; in particular, the contribution of the East Antarctic Ice Sheet (EAIS) is ill defined, restricting our appreciation of potential future change. Several lines of evidence suggest possible collapse of the Totten Glacier into interior basins during past warm periods, most notably the Pliocene epoch<sup>1–4</sup>, causing several metres of sea-level rise. However, the structure and long-term evolution of the ice sheet in this region have been understood insufficiently to constrain past ice-sheet extents. Here we show that deep ice-sheet erosion—enough to expose basement rocks—has occurred in two regions: the head of the Totten Glacier, within 150 kilometres of today’s grounding line; and deep within the Sabrina Subglacial Basin, 350–550 kilometres from this grounding line. Our results, based on ICECAP aerogeophysical data, demarcate the marginal zones of two distinct quasi-stable EAIS configurations, corresponding to the ‘modern-scale’ ice sheet (with a marginal zone near the present ice-sheet margin) and the retreated ice sheet (with the marginal zone located far inland). The transitional region of 200–250 kilometres in width is less eroded, suggesting shorter-lived exposure to eroding conditions during repeated retreat–advance events, which are probably driven by ocean-forced instabilities. Representative ice-sheet models indicate that the global sea-level increase resulting from retreat in this sector can be up to 0.9 metres in the modern-scale configuration, and exceeds 2 metres in the retreated configuration.**

Satellite-based observations indicate that the margin of Totten Glacier may be experiencing greater ice loss than anywhere else in East Antarctica<sup>5,6</sup>. This, coupled with the presence of low-lying subglacial basins upstream<sup>7,8</sup>, means the Totten Glacier catchment area could be at risk of substantial ice loss under ocean-warming conditions. The vulnerability of this region to change might be driven by the entrance of warm modified circumpolar deep water to the Totten Ice Shelf cavity<sup>9,10</sup>, for which bathymetric pathways are known<sup>11</sup>.

Totten Glacier possesses an ice stream that extends far inland<sup>12</sup>. This ice stream mostly overlies the Sabrina Subglacial Basin (SSB), which is a bowl-shaped depression bounded to the east by the Terre Adelie highlands, and to the west and south by the recently discovered Highlands B and C (Fig. 1). This region has widely distributed subglacial hydrology<sup>13</sup> and little large-scale topographic relief<sup>8,13,14</sup>. The SSB is underlain by a sedimentary basin (the SSSB) with moderate but quite variable thickness (Fig. 1c). The SSSB probably dates back to at least 40 million years ago (Ma)<sup>15</sup>, and therefore pre-dates the glaciation of the EAIS.

Here we use geophysical data from the International Collaborative Exploration of the Cryosphere through Airborne Profiling (ICECAP) program (Extended Data Fig. 1) to define the erosion of the SSB by past

EAIS activity. We use two-dimensional gravity modelling along flight lines, and also include estimates of depth to magnetic sources, to understand the thickness of sedimentary rocks in the SSSB (Fig. 1c). The thickness of the SSSB is defined with a typical accuracy of  $\pm 600$  metres.

The gravity-model results show that the base of the SSSB sedimentary basin is tilted towards the south–southeast and extends south-east from the Totten Glacier for more than 500 kilometres. Its base is as deep as  $-4,000$  metres elevation in parts, but is typically shallower (Fig. 1b). The pre-erosion basin structure is not uniquely defined, as the basin top is missing, but the least-eroded areas of the SSSB are at least 3 kilometres thick and have a generally flat-based geometry. Faults define smaller-scale perturbations to this geometry. The Aurora Subglacial Basin (ASB) and Vincennes Subglacial Basin (VSB) regions have much larger thickness uncertainties, and we have not interpreted erosion patterns within these basins.

Thickness trends for the SSSB (Fig. 1c) do not parallel the tectonic structure of the region (Extended Data Fig. 2). Thickness variations are high within tectonic blocks, and thickness trends transgress major tectonic structures<sup>15,16</sup>. This suggests that present-day basin thickness is not dominated by tectonic structure; rather, the SSSB thickness defines distinct patterns that are explained by the erosion of the SSB by the EAIS.

Glacial erosion occurs because of basal sliding, which requires warm-based ice and a driving stress that is sufficient to cause motion<sup>17</sup>. The erosion rate depends primarily on the basal velocity of the ice sheet<sup>17</sup>, and because there is the potential for high velocities at the ice-sheet margin, so there is also the potential for enhanced erosion rates at the margin. Erosion may be selective or distributed. Under selective erosion, deep troughs occur in regions with high basal velocity<sup>17</sup>, but a lateral convergence of ice flux is also required, often focused within pre-existing valleys<sup>18</sup>. Thinner ice promotes selective erosion because highlands are often cold-based and do not exhibit the fast basal velocities necessary for substantial erosion; the same highlands may be warm-based under thicker ice cover, and may exhibit fast basal velocities. As a consequence, larger and thicker ice sheets are more likely to exhibit distributed erosion, whereas smaller and thinner ice sheets are more likely to exhibit selective erosion<sup>19</sup>.

For the SSB we interpret several regions of distinctive erosion (Fig. 1d) on the basis of the morphology of the subglacial surface and the thickness of the SSSB (Extended Data Table 1). These regions define erosion from two distinct quasi-stable EAIS configurations: a ‘modern-scale’ configuration, with a marginal zone near the present-day ice-sheet margin; and a ‘retreated’ configuration, with a marginal zone located far inland.

Cumulative glacial erosion is generally low in elevated coastal regions, including Law Dome, the Knox Coast and the Cape Goodenough region, and erosion is also generally low on the highlands surrounding the SSB and ASB. Ice-sheet models suggest that these

<sup>1</sup>School of Earth and Environment, University of Western Australia, Perth, Western Australia 6008, Australia. <sup>2</sup>Australian Antarctic Division, Kingston, Tasmania 7050, Australia. <sup>3</sup>Antarctic Climate & Ecosystems Cooperative Research Centre, University of Tasmania, Hobart, Tasmania 7005, Australia. <sup>4</sup>University of Texas Institute for Geophysics, University of Texas at Austin, Austin, Texas 78758, USA. <sup>5</sup>Antarctic Research Centre, Victoria University of Wellington, Wellington 6140, New Zealand. <sup>6</sup>GNS Science, Avalon, Lower Hutt 5011, New Zealand. <sup>7</sup>The Grantham Institute and Department of Earth Science and Engineering, Imperial College London, London SW7 2AZ, UK.

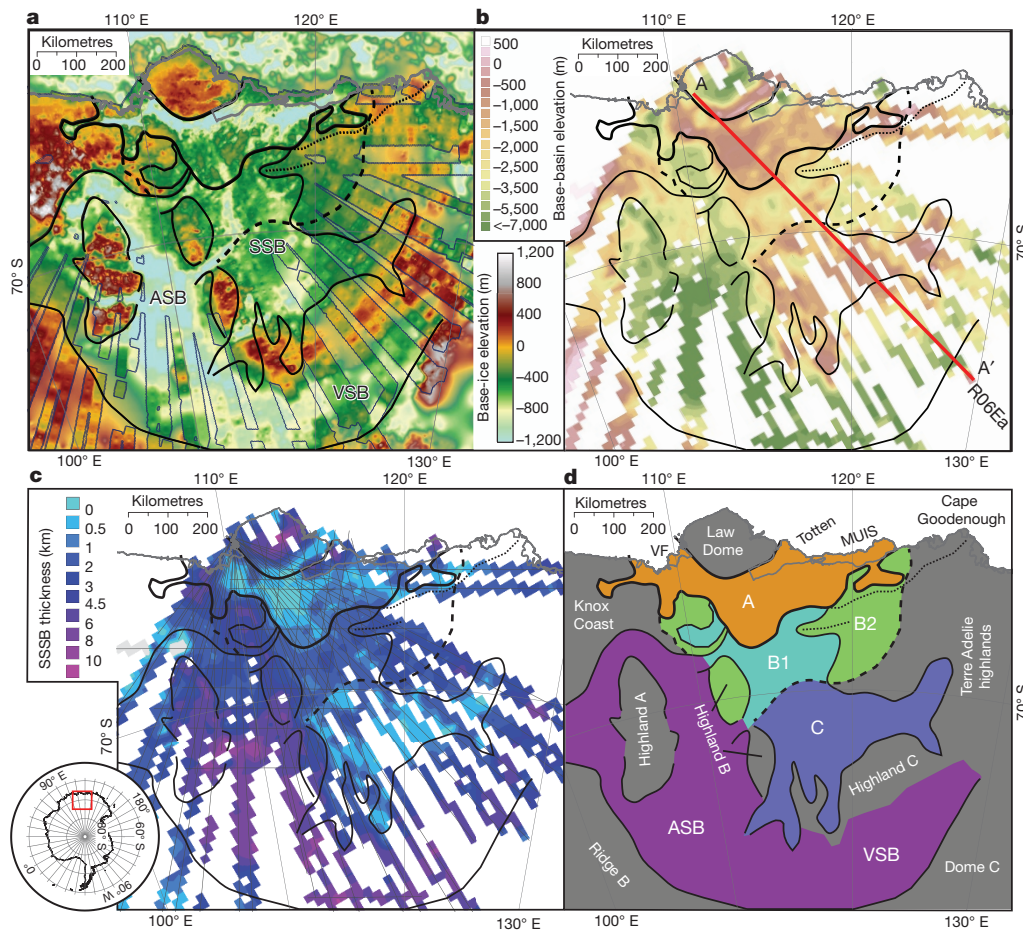


**Figure 1 | Interpretation of erosion in the Sabrina Subglacial Basin region.** The Sabrina Subglacial Basin (SSB) is the low-lying region bounded by Highland B, Highland C and the Terre Adelie highlands. The SSSB is the associated sedimentary basin of moderate thickness. Much thicker sedimentary basins occur in the Aurora Subglacial Basin (ASB) and Vincennes Subglacial Basin (VSB) regions. **a**, Base-ice elevations indicate the ice-sheet bed. Data are from ICECAP and Bedmap2 (ref. 7) (the latter data have a muted appearance). **b**, **c**, The sedimentary-basin base elevation (**b**) and thickness (**c**), both derived from gravity modelling.

Hairlines in **c** show flight lines. **d**, We interpret regions of differing erosion characteristics for the SSB from the elevation and character of subglacial topography and from variations in the preserved thickness of the sedimentary basins (Extended Data Table 1). Heavy solid and dashed lines show the A/B and B/C boundaries, respectively. Thin lines show the interpreted boundaries of the dendritic erosion pattern for regions C and B1. Thin dotted lines indicate the Cape Goodenough Ridge. The inset shows the location of the region within Antarctica. MUIS, Moscow University Ice Shelf; VF, Vanderford Glacier.

highlands generally either are covered with slow-moving ice, or are ice free, with little scope for fast-moving ice (Fig. 3).

Region A surrounds the coastal glaciers, and is a broad region of moderate elevation, cut by a number of smaller channels that align with modern ice-sheet flow<sup>12</sup>. The SSSB thickness is nil for much of region A and rarely exceeds 1 kilometre (Fig. 1c). The A/B boundary is located near a topographic ridge that extends west–southwest from Cape Goodenough. This ridge averages about  $-200$  metres of elevation, but is cut by channels as deep as  $-800$  metres. The ice-sheet bed within region A is ocean sloping, with an average gradient (measured along flight lines) of  $+2$  to  $+4$   $\text{m km}^{-1}$ .

Region B is defined by an almost linear inland-thickening trend to the base of the SSSB, with an upstream limit defined where this thickening trend ceases (Figs 1 and 2). In region B, the thickness of the SSSB increases in co-variance with the reduction in surface ice-sheet velocity (Fig. 2 and Extended Data Figs 3–6). Non-selective and inland-reducing erosion, coupled with the correlation with present-day surface velocity, points to prolonged activity of the modern-scale ice sheet.

Under present climate conditions, ice-sheet modelling indicates high basal velocities within region A (Extended Data Fig. 7a). With an air temperature anomaly,  $dT_{\text{a}}$ , of  $+4^{\circ}\text{C}$  and an ocean temperature anomaly,  $dT_{\text{o}}$ , of  $+1^{\circ}\text{C}$  (anomaly is with respect to present-day temperatures), a retreat of the ice-sheet margin to the A/B boundary is indicated, with

high basal velocities occurring mostly within region B (Fig. 3a). The results of these models suggest that repeated small-scale retreat and advance cycles within region A are necessary to explain the observed erosion. These cycles had a length scale of less than 200 kilometres, did not involve collapse, and were probably orbitally forced<sup>2</sup>.

Region B comprises two subregions. Subregion B2 preserves only the modern-scale ice-sheet-erosion signature, and the SSSB is typically more than 2 kilometres thick. In subregion B1, the SSSB is typically thinner and includes branched channels in addition to the modern-scale ice-sheet signature (Fig. 1). The ice-sheet bed in subregion B1 is beneath sea level and typically inland sloping, with an average gradient of  $-1$  to  $-3$   $\text{m km}^{-1}$ .

Retreat into the SSB from the topographic ridge at the A/B boundary is subject to ocean-driven instabilities. These include the marine ice-sheet instability, moderated by ice-shelf buttressing<sup>20,21</sup>, and ice-cliff failure augmented by hydrofracturing<sup>4</sup>. The former mechanism is widely considered to be the main driver of ice-sheet collapse<sup>21</sup>. The latter mechanism may yield rapid and extensive retreat, although further work is required to verify its role in large-scale ice-sheet collapse<sup>4</sup>.

Following retreat into the SSB interior, a new ice-sheet margin is established in front of Highlands B and C. Region C (Fig. 1) is characterized by sufficient erosion to expose basement, and an overall dendritic pattern. Patches of thicker sedimentary rocks exist between channels.

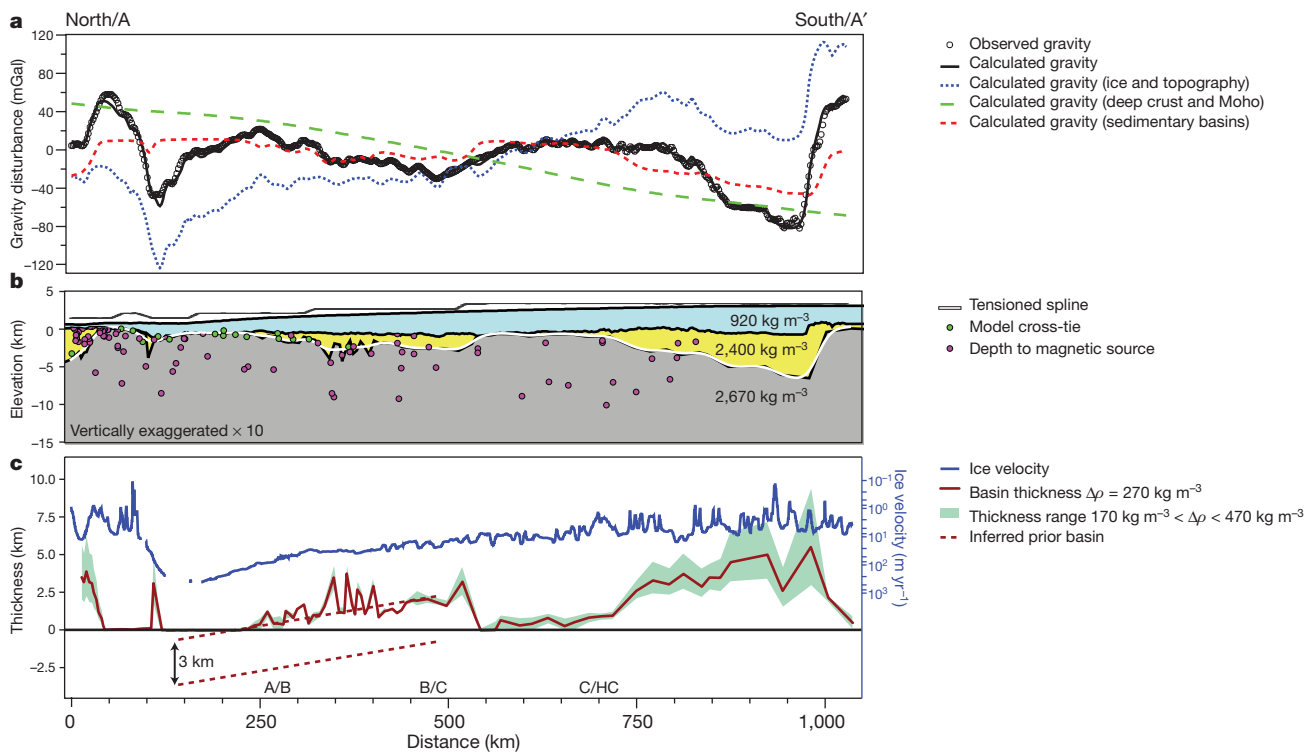


**Figure 2 | Gravity model along flight line R06Ea.** **a**, Observed and calculated gravity disturbances, including model components from ice and topography, the deep crust and Moho, and the sedimentary basins. **b**, Results of the model, showing the thickness of sedimentary rocks required to satisfy the gravity field. Estimates of depth to magnetic source<sup>15</sup>, the tensioned spline fit, and cross-ties with other models are also shown. The gravity disturbance was modelled at true observation elevations, indicated by the uppermost grey line. **c**, SSSB thickness and

present-day surface-ice velocity<sup>12</sup> (vertically flipped; average error in ice-sheet velocity on this line is  $10.5 \text{ m yr}^{-1}$ ). A/B, B/C and C/HC indicate the locations of the interpreted erosion boundaries demarcated in Figs 1 and 3 (HC, Highland C). Dashed lines indicate the inferred prior 3-kilometre thickness of the SSSB, which has been almost entirely removed in region A, and eroded in line with present-day ice velocity in region B. See Extended Data Figs 3–6 for additional representative models throughout the SSB region.

Highland C and the Terre Adelie highlands peak well above sea level, and have average measured gradients on their frontal slopes of about  $+2.5 \text{ m km}^{-1}$ . Consequently, these highlands are persistent barriers to further ice-sheet retreat, even under highly unstable conditions<sup>4,19</sup>.

Highland B, however, is pierced by several deep fjords, which indicate extended periods during which fast ice flow was channelled from a large upstream source in the ASB<sup>8</sup>. The fjords are also where ice-sheet retreat into the ASB is probably initiated. This additional vulnerability limits the residence time of an ice margin in front of Highland B as compared with Highland C<sup>4,8</sup>. Our observed erosion in region B1, which is less than the erosion in region C, suggests that retreat of the EAIS into the ASB has occurred as a characteristic of a fully retreated ice sheet.

The erosion characteristics of regions B1 and C point to the activity of a retreated ice sheet. In our models, when  $dT_a = +8^\circ \text{C}$  and  $dT_o = +2^\circ \text{C}$  (Fig. 3b), the ice-sheet margin retreats to subregion B1, with high basal velocities mostly within subregion B1 and region C. When  $dT_a = +12^\circ \text{C}$  and  $dT_o = +5^\circ \text{C}$ , further retreat to the B/C boundary is suggested (Fig. 3c). This retreat scenario is similar in extent to a previous interpretation<sup>8</sup> of the early ice sheet, before advance into the SSB, although the locations of the ice margins differ. With  $dT_a = +15^\circ \text{C}$  and  $dT_o = +5^\circ \text{C}$ , full retreat into the ASB is indicated (Extended Data Fig. 7b). This retreat scenario is somewhat more extensive than a previous interpretation that considered the early ice sheet, before advance into the ASB<sup>8</sup>.

Overall, the extent of SSB erosion points to long periods of time during which the SSB was subjected to a modern-scale ice sheet, with the margin located within region A (less than 150 kilometres retreat from present), and also large periods of time when it was subjected to a retreated ice sheet, with the margin located much further inland, near the B/C boundary (350 kilometres of retreat from present). Subregion

B1 is apparently less eroded than both regions A and C, suggesting that the residence time of the ice-sheet margin in this region has been less. This may indicate repeated but relatively short-lived transitions between the modern-scale and retreated states.

Our interpretation is not time specific, but global climate and sea-level data suggest that the retreated ice-sheet was predominant in the Oligocene to mid-Miocene, with the modern-scale ice-sheet predominant since the mid-Miocene<sup>22</sup>. Corresponding detrital provenance records at Prydz Bay<sup>1</sup> and locally in sediment cores<sup>23</sup> suggest that basement rocks were being eroded from region A at 7 Ma and at 3.5 Ma (ref. 1). Therefore, the modern-scale ice-sheet has been a recurrent feature of Totten Glacier since well before 7 Ma.

It has been suggested that a substantial Pliocene retreat here may have been necessary to generate the estimated high sea level of up to  $22 \pm 10$  metres above present<sup>24</sup>, although a recent estimate is more moderate, at 9–13.5 metres; ref. 25. Our data cannot directly constrain the extent of the Pliocene ice sheet at Totten Glacier, but we can estimate the contribution of this sector to global sea level for our representative ice-sheet models.

Prior reconstructions of retreat from a modern-scale configuration under Pliocene conditions are highly variable<sup>26</sup>. Models with a highly unstable ice sheet<sup>4,26,27</sup> can retreat markedly, while more stable ice-sheet reconstructions typically fail to do so<sup>26,28</sup>. Furthermore, different ice-sheet models can resolve similar ice-sheet extents with differing amounts of sea-level contribution<sup>4,26</sup>. There might also be short-term sea-level fluctuations that we do not consider here<sup>29</sup>.

The largest retreat possible under the modern-scale ice-sheet configuration (Fig. 3a) is associated with a total Antarctic sea-level contribution of 8.39 metres, of which the SSB/ASB sector provides 0.89 metres. Even allowing for 7.3 metres of sea-level increase from collapse of the Greenland ice sheet<sup>30</sup>, this is insufficient to explain 22 metres of total

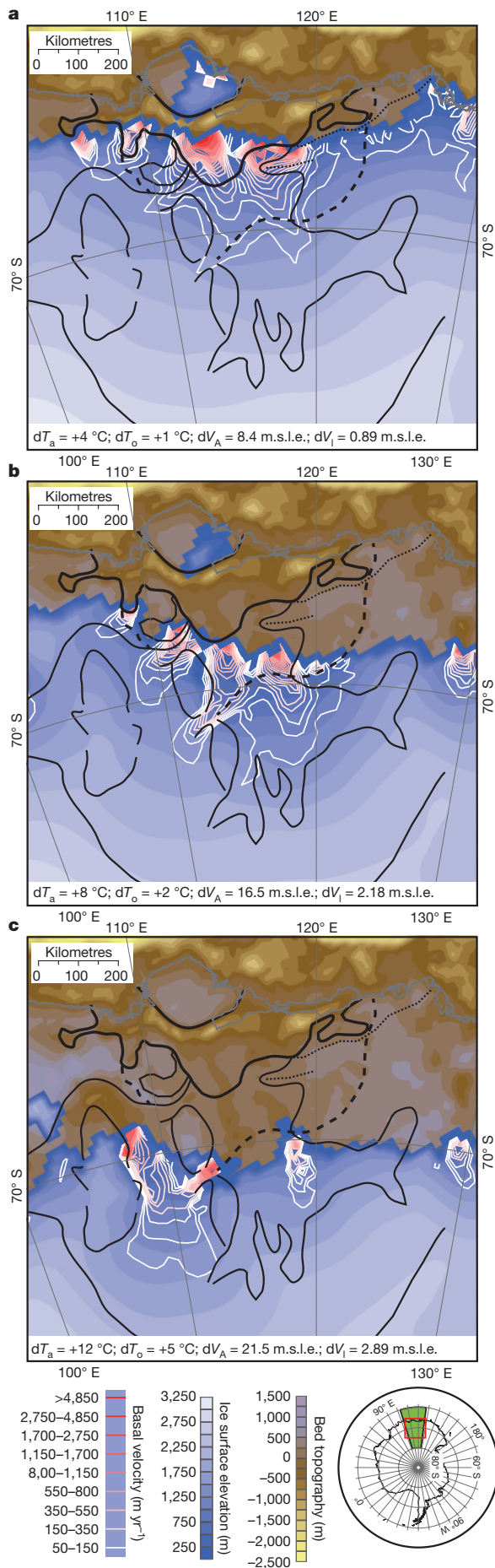


**Figure 3 | Ice-sheet models with differing climate forcings.** Ice-sheet surface and bed elevations and basal velocity contours are shown after a long-term 20,000-year run under constant climate forcing. Models were run with air temperatures ( $dT_a$ ) and ocean temperatures ( $dT_o$ ) above today's. Contributions to global-mean sea level are estimated for all Antarctica ( $dV_A$ ) and for the SSB/ASB sector ( $dV_I$ ; indicated by the green area in the inset). **a**, With  $dT_a = +4\text{ }^\circ\text{C}$  and  $dT_o = +1\text{ }^\circ\text{C}$ , the ice-sheet margin is located near the A/B boundary and high basal velocities are focused in region B. **b**, With  $dT_a = +8\text{ }^\circ\text{C}$  and  $dT_o = +2\text{ }^\circ\text{C}$ , the ice-sheet margin is located in region B and high basal velocities are focused in regions B1 and C. **c**, With  $dT_a = +12\text{ }^\circ\text{C}$  and  $dT_o = +5\text{ }^\circ\text{C}$ , the ice-sheet margin is located near the B/C boundary and high basal velocities are focused in region C and the ASB. Further models are shown in Extended Data Fig. 7. m.s.l.e., metres of sea-level equivalent.

sea-level rise<sup>24</sup>, but it is sufficient to explain an increase of 13.5 metres (ref. 25).

Our two models of the retreated ice sheet state (Fig. 3b, c) are associated with a total Antarctic sea-level contribution of 16.5 metres or 21.5 metres, of which the SSB/ASB sector provides 2.18 metres and 2.89 metres, respectively. Retreat of the ice sheet into the ASB (Extended Data Fig. 7b) is associated with a total Antarctic sea-level contribution of 29.1 metres, with 4.29 metres sourced from the SSB/ASB sector.

The influence of Totten Glacier on past sea level is clearly notable, but for any particular warm period it is also highly uncertain, because the system is subject to progressive instability. Our results suggest that the first discriminant is the development of sufficient retreat to breach the A/B-boundary ridge. This causes an instability-driven transition from the modern-scale configuration to the retreated configuration. Under ongoing ice-sheet loss, the breaching of Highland B causes further retreat into the ASB. Each of these changes in state is associated with a substantial increase in both the absolute and the proportional contribution of this sector to global sea level.

**Online Content** Methods, along with any additional Extended Data display items and Source Data, are available in the online version of the paper; references unique to these sections appear only in the online paper.

**Received 9 September 2015; accepted 16 February 2016.**

- Williams, T. *et al.* Evidence for iceberg armadas from East Antarctica in the Southern Ocean during the late Miocene and early Pliocene. *Earth Planet. Sci. Lett.* **290**, 351–361 (2010).
- Patterson, M. O. *et al.* Orbital forcing of the East Antarctic ice sheet during the Pliocene and Early Pleistocene. *Nature Geosci.* **7**, 841–847 (2014).
- Cook, C. P. *et al.* Dynamic behaviour of the East Antarctic ice sheet during Pliocene warmth. *Nature Geosci.* **6**, 765–769 (2013).
- Pollard, D., DeConto, R. M. & Alley, R. B. Potential Antarctic Ice Sheet retreat driven by hydrofracturing and ice cliff failure. *Earth Planet. Sci. Lett.* **412**, 112–121 (2015).
- Pritchard, H. D., Arthern, R. J., Vaughan, D. G. & Edwards, L. A. Extensive dynamic thinning on the margins of the Greenland and Antarctic ice sheets. *Nature* **461**, 971–975 (2009).
- Rignot, E., Jacobs, S., Mouginot, J. & Scheuchl, B. Ice shelf melting around Antarctica. *Science* **341**, 266–270 (2013).
- Fretwell, P. *et al.* Bedmap2: improved ice bed, surface and thickness datasets for Antarctica. *Cryosphere* **7**, 375–393 (2013).
- Young, D. A. *et al.* A dynamic early East Antarctic Ice Sheet suggested by ice-covered fjord landscapes. *Nature* **474**, 72–75 (2011).
- Gwyther, D. E., Galton-Fenzi, B. K., Hunter, J. R. & Roberts, J. L. Simulated melt rates for the Totten and Dalton ice shelves. *Ocean Science* **10**, 267–279 (2014).
- Khazendar, A. *et al.* Observed thinning of Totten Glacier is linked to coastal polynya variability. *Nature Commun.* **4**, 2857 (2013).
- Greenbaum, J. S. *et al.* Ocean access to a cavity beneath Totten Glacier in East Antarctica. *Nature Geosci.* **8**, 294–298 (2015).
- Rignot, E., Mouginot, J. & Scheuchl, B. Ice flow of the Antarctic ice sheet. *Science* **333**, 1427–1430 (2011).
- Wright, A. P. *et al.* Evidence of a hydrological connection between the ice divide and ice sheet margin in the Aurora Subglacial Basin, East Antarctica. *J. Geophys. Res. Earth Surface* **117**, F01033 (2012).
- Roberts, J. L. *et al.* Refined broad-scale sub-glacial morphology of Aurora Subglacial Basin, East Antarctica derived by an ice-dynamics-based interpolation scheme. *Cryosphere* **5**, 551–560 (2011).
- Aitken, A. R. A. *et al.* The subglacial geology of Wilkes Land, East Antarctica. *Geophys. Res. Lett.* **41**, 2390–2400 (2014).

16. Aitken, A. R. A. *et al.* The Australo-Antarctic Columbia to Gondwana transition. *Gondwana Res.* **29**, 136–152 (2016).
17. Drewry, D. J. *Glacial Geologic Processes* (Edward Arnold, 1986).
18. Rose, K. C. *et al.* Early East Antarctic Ice Sheet growth recorded in the landscape of the Gamburtsev Subglacial Mountains. *Earth Planet. Sci. Lett.* **375**, 1–12 (2013).
19. Jamieson, S. S. R., Sugden, D. E. & Hulton, N. R. J. The evolution of the subglacial landscape of Antarctica. *Earth Planet. Sci. Lett.* **293**, 1–27 (2010).
20. Gudmundsson, G. H. Ice-shelf buttressing and the stability of marine ice sheets. *Cryosphere* **7**, 647–655 (2013).
21. Joughin, I. & Alley, R. B. Stability of the West Antarctic ice sheet in a warming world. *Nature Geosci.* **4**, 506–513 (2011).
22. Flower, B. P. & Kennett, J. P. The middle Miocene climatic transition: East Antarctic ice sheet development, deep ocean circulation and global carbon cycling. *Palaeogeogr. Palaeoclimatol. Palaeoecol.* **108**, 537–555 (1994).
23. Pierce, E. L. *et al.* Characterizing the sediment provenance of East Antarctica's weak underbelly: the Aurora and Wilkes sub-glacial basins. *Paleoceanography* **26**, PA4217 (2011).
24. Miller, K. G. *et al.* High tide of the warm Pliocene: implications of global sea level for Antarctic deglaciation. *Geology* **40**, 407–410 (2012).
25. Winnick, M. J. & Caves, J. K. Oxygen isotope mass-balance constraints on Pliocene sea level and East Antarctic Ice Sheet stability. *Geology* **43**, 879–882 (2015).
26. de Boer, B. *et al.* Simulating the Antarctic ice sheet in the late-Pliocene warm period: PLISMIP-ANT, an ice-sheet model intercomparison project. *Cryosphere* **9**, 881–903 (2015).
27. Gasson, E., DeConto, R. & Pollard, D. Antarctic bedrock topography uncertainty and ice sheet stability. *Geophys. Res. Lett.* **42**, 5372–5377 (2015).
28. Pollard, D. & DeConto, R. M. Modelling West Antarctic Ice Sheet growth and collapse through the past five million years. *Nature* **458**, 329–332 (2009).
29. Golledge, N. R. *et al.* The multi-millennial Antarctic commitment to future sea-level rise. *Nature* **526**, 421–425 (2015).
30. Alley, R. B. *et al.* History of the Greenland Ice Sheet: paleoclimatic insights. *Quat. Sci. Rev.* **29**, 1728–1756 (2010).

**Acknowledgements** Collection of ICECAP data was supported by: National Science Foundation grant PLR-0733025; National Aeronautics and Space Administration grants NNX09AR52G, NNG10HP06C and NNX11AD33G (Operation Ice Bridge and the American Recovery and Reinvestment Act); Australian Antarctic Division projects 3013 and 4077; National Environment and Research Council grant NE/D003733/1; the Jackson School of Geosciences; the G. Unger Vetlesen Foundation; and the Australian Government's Cooperative Research Centres Programme through the Antarctic Climate & Ecosystems Cooperative Research Centre (ACE CRC). Ice-sheet modelling was funded under contract VUW1203 of the Royal Society of New Zealand's Marsden Fund. We thank S. Jamieson for comments and for supplying model images for comparison. This is the University of Texas Institute of Geophysics contribution 2950.

**Author Contributions** A.R.A.A. undertook data processing, analysis and modelling and wrote the paper. D.D.B., T.D.v.O. and M.J.S. coordinated and planned the fieldwork and led the ICECAP programme. J.L.R., D.A.Y. and J.S.G. undertook the field program and implemented data collection, quality control and initial data processing. N.R.G. conducted the ice-sheet modelling. All authors contributed significantly to interpretation and discussion of the data and manuscript preparation.

**Author Information** Reprints and permissions information is available at [www.nature.com/reprints](http://www.nature.com/reprints). The authors declare no competing financial interests. Readers are welcome to comment on the online version of the paper. Correspondence and requests for materials should be addressed to A.R.A.A. ([alan.aitken@uwa.edu.au](mailto:alan.aitken@uwa.edu.au)).

## METHODS

**Data.** Aerogeophysical data used include ice-surface, ice-thickness, magnetic and gravity data, all of which were collected through the ICECAP program during Antarctic summer seasons 2009/2010 through to 2012/2013. Instruments were flown aboard the DC-3T aircraft, civil registered as C-GJKB, owned and operated by Kenn Borek Air. Line data for these ICECAP products are available at full resolution through the ICEBRIDGE data portal at the National Snow and Ice Data Center (<http://nsidc.org/icebridge/portal/>).

The ice-surface elevation was obtained using a Riegl LD90-3800-HiP-LR laser ranging system, combined with a range of GPS receivers and inertial measurement unit (IMU) systems. Spatial resolution is 25 m along track and 1 m across track, with a net error of approximately 12 cm (ref. 31). Ice thickness was determined with the 60 MHz HiCARS ice-penetrating radar system<sup>32</sup>. Crossovers in ice thickness yield an average difference of approximately 33 m (ref. 8); crossover difference scales as a function of basal roughness up to a few hundred metres. This error is due predominantly to uncertainty in the horizontal location of the reflection point, which occurs within a radius of about 500 m.

Magnetic intensity data were measured with a Geometrics G-823A caesium vapour magnetometer housed in an aircraft tailboom<sup>33</sup>. Raw total magnetic intensity data are reduced to magnetic intensity anomalies by correcting for the International Geomagnetic Reference Field, time variations in magnetic field, and spline-based line levelling<sup>15</sup>.

For the first three seasons, gravitational acceleration data were obtained with a Bell Aerospace BGM-3, two-axis-stabilized scalar gravity meter<sup>34</sup>. Gravitational acceleration was sampled at 1 Hz. Aircraft vertical and horizontal accelerations were estimated using dual carrier phase GPS solutions, and removed from the observed accelerations before filtering. A symmetrical finite impulse response low-pass filter with half-amplitude frequency point of 0.0054 Hz (185 s) was used to smooth the resulting data. In the 2012/2013 season, the BGM-3 gravity meter was replaced with a three-axis-stabilized Canadian Microgravity GT-1A system<sup>35</sup>. Gravitational acceleration was sampled at an effective sampling rate of 18.75 Hz, and filtered with a filter length of 150 s (0.006667 Hz). Typical aircraft velocity was 90 m s<sup>-1</sup>, so this results in a minimum resolvable half-wavelength of approximately 8 km for BGM-3 data and 6.75 km for GT-1A data.

The gravitational acceleration data were automatically edited on the basis of horizontal and vertical acceleration thresholds, and corrected for latitude, instrument drift, elevation, and the Eotvös effect. The final result is the disturbance from the global gravity field, or gravity disturbance. This is equivalent to the free-air anomaly.

**Gravity modelling approach and model uncertainty.** For gravity modelling, we used the gravity disturbance data, with vertical gravitational accelerations calculated at observation elevation. For modelling along flight lines, we used an iterative combination of forward modelling and inversion, using the commercial two-dimensional code GM-sys which is based upon the principles of ref. 36. Full three-dimensional modelling is not appropriate for our survey design, owing to the sparse and irregularly spaced data and variably oriented flight lines.

An initial model, described below, was perturbed using an iterative combination of inversion and manual forward modelling. The boundaries of the sedimentary basin base were inverted for depth using the inbuilt GM-sys inversion module, which uses a damped least-squares optimization<sup>37</sup> to estimate the thickness of the basin that minimizes gravity misfit. Inversion damping is not user specified, and results can be erratic. Therefore, in between inversion iterations, we carried out manual editing involving smoothing of anomalously steep or erratic results, and corrections so as to better match the ice-sheet-bed morphology where the thickness is close to zero. Most results were achieved within two or three iterations.

This approach can successfully be used to model one-dimensional and two-dimensional structures, but not complex three-dimensional structures. Our approach is valid for the ice-sheet surface and the SSSB base, which are very close to one-dimensional, but some topographic features are three dimensional in form. In addition, we only resolve gravity features with widths of more than 6.75–8 km, whereas the ice-sheet bed is resolved at a much finer detail. Our models represent this topography with a data spacing of roughly 2 km. Combining the above leads to inaccurate basin-thickness models near rugged topography—such regions including the edges of Highland A, fjords, and deep channels. These regions are also most likely to possess large errors in the subglacial topography data set. In elevation terms, these errors are on average an order of magnitude less than our gravity modelling error, but in gravity terms they might be important owing to the high density contrast at this interface (~1,500 kg m<sup>-3</sup> versus ~300 kg m<sup>-3</sup>).

We constructed an initial model consisting of five layers: ice sheet, sedimentary basins, upper crust, lower crust and mantle. These layers exist, in order, across the entire model and cannot overlap, although they can become zero thickness. Boundaries for the ice-sheet surface and bed elevations were derived directly from the ICECAP line data, and for the ice sheet we used a density of 920 kg m<sup>-3</sup>. Density

variations from the ice-sheet surface and bed are the most notable component of the gravity disturbance data (Fig. 2 and Extended Data Figs 3–6). The Moho was defined by a flexural model that accounts for ice and topographic loads. An elastic thickness of 25 km was used, although—because of the long-wavelength of the loads involved—little variation in Moho structure is observed between 10 km and 50 km elastic thickness. The lower crust had a density of 2,800 kg m<sup>-3</sup>, the mantle a density of 3,200 kg m<sup>-3</sup>. Density variations from these interfaces largely balance out the long-wavelength gravity effects of ice-thickness and topography variations (Fig. 2 and Extended Data Figs 3–6). None of these layer boundaries was a variable in the gravity model.

Our target interface for modelling is the base of the sedimentary basins. We precondition the model using previously published depth-to-magnetic-source estimates from the ICECAP data set<sup>15</sup>. These source points were derived from multiple passes of Werner deconvolution<sup>38</sup> using the levelled magnetic line data. As an initial surface, we infer the base of the sedimentary basin at the uppermost resolved magnetic source, under the condition that the slope of the basin base was not excessive. Where the bed is typically deep, we ignored responses at the ice-sheet bed. Substantial scatter is evident in the depth-to-source estimates, but nonetheless they define the overall geometries of the SSSB and the sedimentary basins in the ASB and VSB<sup>15</sup>. Except for initializing the geometry of this surface, we did not use the depth-to-magnetic-source estimates to constrain the geometry of the returned model surface.

We assumed, in the first instance, a crystalline basement density of 2,670 kg m<sup>-3</sup>. Sedimentary rock density was varied between a lower limit of 2,200 kg m<sup>-3</sup> and an upper limit of 2,500 kg m<sup>-3</sup>, providing an effective density contrast range of 300 kg m<sup>-3</sup>. The lower limit was based on a reasonable maximum porosity of 25%, given the thickness of ice and the likely age of the rocks; the upper limit was defined by the point at which basin thickness departs considerably from magnetic depth-to-basement estimates<sup>15</sup>. These sedimentary densities provide the largest uncertainty regarding basin thickness and create the ranges of sediment thickness shown in Fig. 2c and Extended Data Figs 3c, 4c, 5c and 6c. In the deeper parts of the SSB, the ASB and VSB, this uncertainty can approach several kilometres. Along-line analyses for our selected profiles give a length-weighted mean uncertainty of ±1,239 m, but the length-weighted mean value for the SSB region is ±609 m. Although large, the error is a systematic uncertainty that varies linearly and predictably with basin thickness, and has no influence on the pattern of basin thickness, only the magnitude. Consequently, our interpreted erosion boundaries are not especially sensitive to this uncertainty, but estimates of the amount of erosion are.

A limitation of the gravity method is that only relative gravity differences are modelled, and results for each line are not directly comparable. To correct for this, we levelled the results to a common baseline. We reduced cross-line differences by applying a constant value to a tensioned spline fit through the basin base on each line, so as to minimize the misfit between that line and all cross-ties. These cross-ties (Extended Data Fig. 8) have a mean cross-tie difference—that is, the total difference in thickness—of 607 m (or ±303.5 m), and a median cross-tie difference of 417 m (or ±208.5 m). The highest values are associated with rugged topography, certain flight lines, and the deepest basin regions. Some lines traverse long sections without cross-ties, in particular at the ends of the lines. It is hard to numerically assess the effect of the lack of tie-points; however, the isolated intersections at the south of the image do not show atypical error, although they are above average (Extended Data Fig. 8). The central SSB provides consistently low cross-line differences (Extended Data Fig. 8). This error encapsulates most of the non-systematic errors in the gravity modelling, including those associated with gravity data accuracy, inversion instabilities, three-dimensional gravity effects, topographic errors, and undersampling of small features. The cross-tie errors suggest that, for a particular density contrast, the sedimentary basin thickness can usually be defined to within ±300 m.

A final consideration is the potential influence of lateral variations in density within the region. We note that the gravity data contain the summed gravity field of all sources. Thus we have the fundamental ambiguity that, for any given lateral density distribution, a basin thickness could be found to satisfy the gravity field, and vice versa. In the absence of firm information on these lateral variations, we have adopted a simple approach to modelling the thickness of sedimentary rocks. Nevertheless, lateral variations in density are undoubtedly present. Lateral variations in sedimentary rock density will occur within the previously defined bounds unless they are highly unusual. Basement density variations may also be important, and can be classed either as intra-block or inter-block variability.

Intra-block variability is hard to predict and to test, and cannot be excluded here, but typically is not a major influence on the large-scale gravity field unless large mafic intrusions exist. The error from internal block variability may be comparable in magnitude, but not in pattern, to the variability in sedimentary basin density. For example, a large, 5-km-thick tabular body with a density contrast of 50 kg m<sup>-3</sup> is equivalent to a ±500 m uncertainty in basin thickness with density

contrast of  $250 \text{ kg m}^{-3}$ . In the case of the SSSB, the observed intra-block gravity variations show correlation with the subglacial topography, which includes fairly well defined glacial landscapes, and, for regions A and B, correlates also with the present ice-sheet velocity. An igneous or metamorphic explanation demands an unlikely coincidence, and so we consider it unlikely that basement density variations are the main source of intra-block gravity variability.

Inter-block density variations are potentially more important. Owing to the size and depth extent of crustal blocks, even small variations between them can be substantial. Extended Data Fig. 1 shows that the SSB region possesses a large gravity disturbance high, whereas the Aurora and Vincennes Subglacial Basin regions possess large gravity disturbance lows. The Knox Coast and Law Dome have relatively high gravity, and the Terre Adelie highlands are mixed in response. Tectonic interpretations based predominantly on magnetic data, but also on gravity data<sup>15</sup>, indicate that in this region there are several major tectonic structures—including the Totten Shear Zone, along Totten Glacier; the Aurora Fault and the Indo-Australo-Antarctic Suture, which bound the ASB to the northwest and southeast respectively; and the Frost Fault, which bounds the Terre Adelie highlands. Several unnamed faults subdivide the Mawson Craton<sup>15</sup>.

A recent model of Australia's crust<sup>39</sup> returns vertically averaged crustal density anomalies for the comparable region that range from  $+0.2\%$  to  $+3.8\%$ , with a mean of  $+2.0\%$  and a standard deviation ( $\sigma$ ) of  $0.58\%$ . Applying those  $2\sigma$  limits with a base density value of  $2,670 \text{ kg m}^{-3}$ , the overall basement density range is approximately  $60 \text{ kg m}^{-3}$ . We test the impact of a comparable density range on our basin models by applying reasonable basement density contrasts of  $\pm 25 \text{ kg m}^{-3}$ . Models along flight lines R03Ea, R06Ea and R08Eb allow comparison with the unperturbed models (Fig. 2 and Extended Data Figs 4, 5). The Y07b and GL0092a lines did not cross sufficient major faults to be included here.

Within these models, each major crustal block is assigned a density of  $2,670 \text{ kg m}^{-3}$ ,  $2,645 \text{ kg m}^{-3}$  or  $2,695 \text{ kg m}^{-3}$ . To test our models' robustness, we seek the density configuration within these bounds that leads to the flattest basin morphology (Extended Data Fig. 9). Models were inverted once, with no subsequent smoothing, so the results are slightly more rugged than the initial geometry (Extended Data Fig. 9). Automated adjustment of data shift was applied, and so even blocks without changes to density contrast can have changed basin geometries.

Under this testing, substantial changes are made to the VSB and Terre Adelie regions, and to the thickness variation between these regions and the SSB. For the VSB and ASB regions, and for the Terre Adelie region, it is likely that inter-block basement density variations contribute to the gravity anomaly, although it is not known to what extent. This, combined with the large thickness of the basins, raises uncertainty as to the basin geometry.

For the SSB, which is now underlain by a dense crustal block, substantial changes to thickness are observed, but the pattern of basin thickness remains similar (Extended Data Fig. 9). In particular, the inland slope within regions A and B and the contrast between regions B1 and C are persistent features. The A/B boundary shows no correlation with any major tectonic boundary. On line R08Eb, and to a lesser degree on line R06Ea, the B/C boundary is correlated with a notable basement fault. Such a correlation is consistent with the overdeepening of a fault-related topographic depression during glacial activity, and also with the subsequent influence of fjord formation on EAIS erosion. This link with basement structure does not necessarily imply that the observed thickness variations are tectonic in origin. The same fault does not correlate to a significant thickness variation on line R03Ea.

**Ice-sheet modelling.** We follow an established methodology in our experiments<sup>29</sup>, and adopt the same present-day input climatology and tuning parameters (stress balance and basal resistance prescription). The following aspects of our new experiments differ, however. Our experiments start from a thermally equilibrated ice-sheet geometry and run for 20,000 years (20 kyr), so that the modelled ice-sheet is at (or close to) equilibrium. Climate perturbations are applied as linear changes from present-day conditions, between 2,000 and 3,000 model years. The first 2,000 years allow any transient behaviour associated with model initialization to take place in the absence of environmental perturbations, whereas the subsequent 1,000 years force the ice sheet to evolve slowly to changes in air and ocean temperatures and precipitation. The remaining 17 kyr allow a steady state to be reached. All experiments are run at a spatial resolution of 20 km.

As previously<sup>29</sup>, we use a sub-grid-scale basal-traction and driving-stress interpolation scheme to allow realistic grounding-line motion<sup>40</sup>. However, we choose not to implement the sub-grid-scale interpolated ice-shelf basal melt component of this scheme, owing to uncertainties as to its validity and the possible resolution dependence of model results<sup>29,41</sup>. Calving is parameterized using horizontal strain rates and a minimum thickness criterion<sup>42,43</sup>.

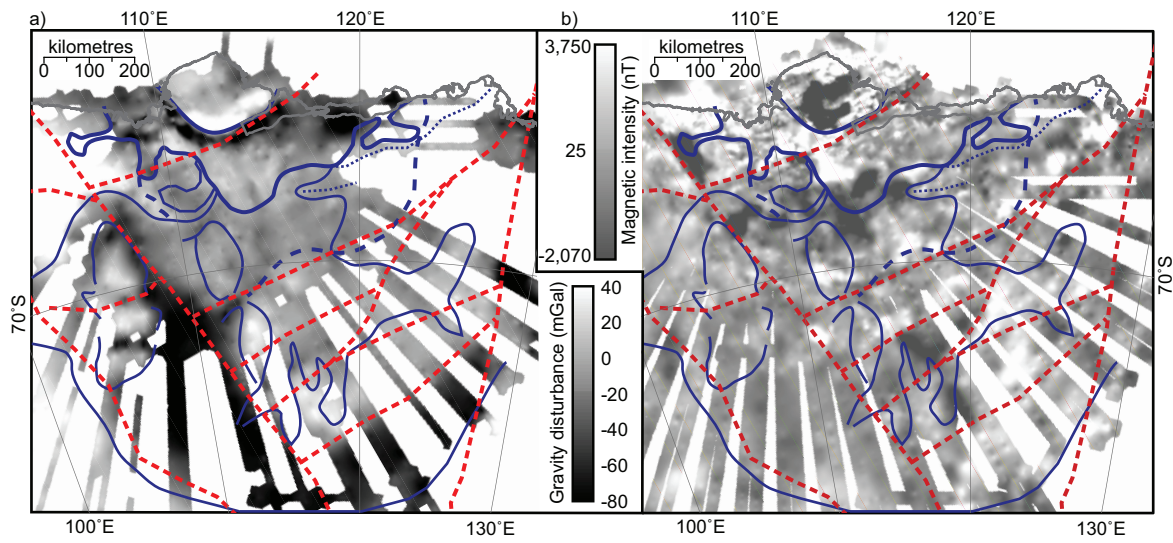
Surface mass balance depends on monthly climatological data and a positive degree-day model that tracks snow thickness and allows for melting of snow

and ice at  $3 \text{ mm } ^\circ\text{C}^{-1} \text{ day}^{-1}$  and  $8 \text{ mm } ^\circ\text{C}^{-1} \text{ day}^{-1}$  respectively. We incorporate a white-noise signal (normally distributed; mean random temperature increment of zero) into the calculation of daily temperature variations. The standard deviation of daily temperature variability is set at  $2^\circ\text{C}$ , somewhat lower than the commonly used value of  $5^\circ\text{C}$ , on the basis that the latter has a tendency to overestimate melt<sup>44,45</sup>. Surface temperatures are adjusted for elevation according to an altitudinal lapse rate of  $-8 \text{ K km}^{-1}$ , and a refreezing coefficient of 0.6 is used to mimic meltwater capture within the snowpack.

The sea-level contribution for the whole of Antarctica is derived directly from the numerical ice-sheet model<sup>29</sup>. For the Aurora and Sabrina basins sector, we derive the relative sea-level contribution within the region defined by the longitudinal limits of  $102.5^\circ\text{E}$  and  $127.5^\circ\text{E}$ , and north of  $80^\circ\text{S}$ . These limits encompass the Totten Glacier catchment, with minimal effects from including parts of adjacent regions. We extend the region north into the ocean  $60^\circ\text{S}$  so as to capture any isostatic bathymetric effects offshore. For each model result, we compute the remaining mass-loss potential, defined by the difference between the mass of the ice sheet, and the mass of water required to inundate regions below sea level. The difference in mass-loss potential between models returns the mass that has been lost or gained. This mass difference was converted to an equivalent seawater volume, and divided by the global ocean area ( $3.6 \times 10^{14} \text{ m}^2$ ) to estimate global sea-level change. For consistency in resolution, we use the model with present-day climate forcing as the baseline, rather than the present-day ice sheet.

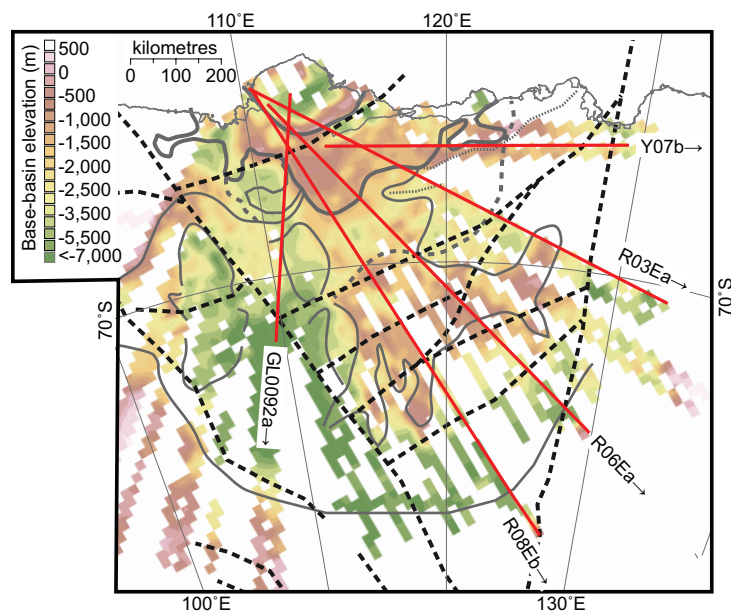
**Code availability.** All geophysical processing and modelling used commercially available software, including ArcGIS from ESRI and Oasis Montaj from Geosoft. Ice-sheet modelling used the PISM code which is available from <https://github.com/pism/pism>.

31. Blankenship, D. D. *et al.* IceBridge Riegl Laser Altimeter L2 Geolocated Surface Elevation Triplets, version 1. NASA Distributed Active Archive Center (DAAC) at the National Snow and Ice Data Center (NSIDC) <http://dx.doi.org/10.5067/JV9DENETK13E> (NASA DAAC NSIDC, 2012, updated 2013).
32. Blankenship, D. D., Kempf, S. D. & Young, D. A. IceBridge HiCARS 2 L2 Geolocated Ice Thickness, version 1. NASA Distributed Active Archive Center (DAAC) at the National Snow and Ice Data Center (NSIDC) <http://dx.doi.org/10.5067/9EBR2TOVXUDG> (NASA DAAC NSIDC, 2012, updated 2013).
33. Blankenship, D. D., Kempf, S. D. & Young, D. A. IceBridge Geometrics 823A Cesium Magnetometer L1B Time-Tagged Magnetic Field, version 1. NASA Distributed Active Archive Center (DAAC) at the National Snow and Ice Data Center (NSIDC) <http://dx.doi.org/10.5067/9WRB1GVWBU70> (NASA DAAC NSIDC, 2011, updated 2013).
34. Blankenship, D. D., Young, D. A., Richter, T. G. & Greenbaum, J. S. IceBridge BGM-3 Gravimeter L2 Geolocated Free Air Anomalies. NASA Distributed Active Archive Center (DAAC) at the National Snow and Ice Data Center (NSIDC) <http://dx.doi.org/10.5067/8DJW56PKY133> (NASA DAAC NSIDC, 2011, updated 2014).
35. Blankenship, D. D., Young, D. A., Richter, T. G. & Greenbaum, J. S. IceBridge CMG GT-1A Gravimeter L2 Geolocated Free Air Gravity Disturbances. NASA Distributed Active Archive Center (DAAC) at the National Snow and Ice Data Center (NSIDC) <http://dx.doi.org/10.5067/3X4CIKKSQRU> (NASA DAAC NSIDC, 2014).
36. Talwani, M. Computation with the help of a digital computer of magnetic anomalies caused by bodies of arbitrary shape. *Geophysics* **30**, 797–817 (1965).
37. Webring, M. SAKI: a Fortran program for generalized linear inversion of gravity and magnetic profiles. US Geol. Surv. Open-File Report 85-122, <http://pubs.usgs.gov/of/1985/0122/report.pdf> (1985).
38. Ku, C. C. & Sharp, J. A. Werner deconvolution for automated magnetic interpretation and its refinement using Marquardt's inverse modeling. *Geophysics* **48**, 754–774 (1983).
39. Aitken, A. R. A., Salmon, M. L. & Kennett, B. L. N. Australia's Moho: a test of the usefulness of gravity modelling for the determination of Moho depth. *Tectonophysics* **609**, 468–479 (2013).
40. Feldmann, J., Albrecht, T., Khroulev, C., Pattyn, F. & Levermann, A. Resolution-dependent performance of grounding line motion in a shallow model compared with a full-Stokes model according to the MISIP3d intercomparison. *J. Glaciol.* **60**, 353–360 (2014).
41. Martin, M. A., Levermann, A. & Winkelmann, R. Comparing ice discharge through West Antarctic Gateways: Weddell vs. Amundsen Sea warming. *Cryosphere Discuss.* **9**, 1705–1733 (2015).
42. Albrecht, T. & Levermann, A. Fracture field for large-scale ice dynamics. *J. Glaciol.* **58**, 165–176 (2012).
43. Levermann, A. *et al.* Kinematic first-order calving law implies potential for abrupt ice-shelf retreat. *Cryosphere* **6**, 273–286 (2012).
44. Seguinot, J. Spatial and seasonal effects of temperature variability in a positive degree-day glacier surface mass-balance model. *J. Glaciol.* **59**, 1202–1204 (2013).
45. Rogozhina, I. & Rau, D. Vital role of daily temperature variability in surface mass balance parameterizations of the Greenland ice sheet. *Cryosphere* **8**, 575–585 (2014).



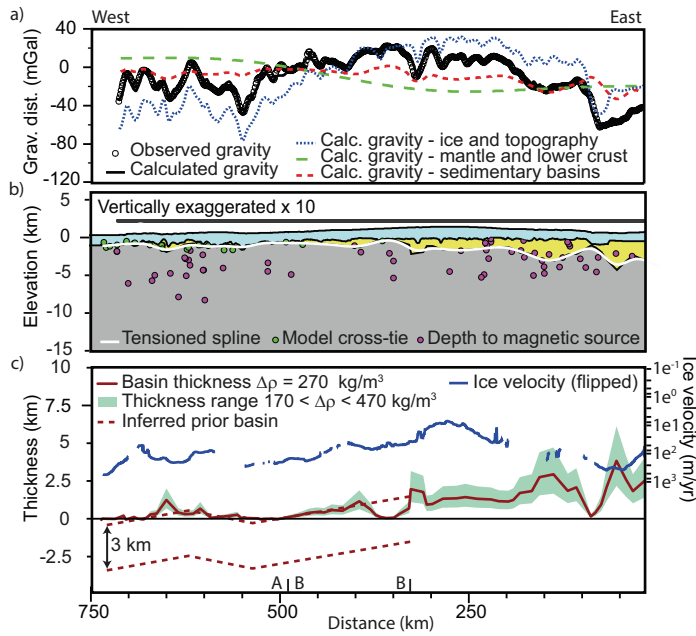
**Extended Data Figure 1 | ICECAP geophysical data. a,** Gravity disturbance data. **b,** Magnetic intensity data. Dashed red lines indicate interpreted basement faults<sup>15</sup>. Solid, dashed and dotted blue lines indicate the erosion interpretation as shown in Fig. 1.





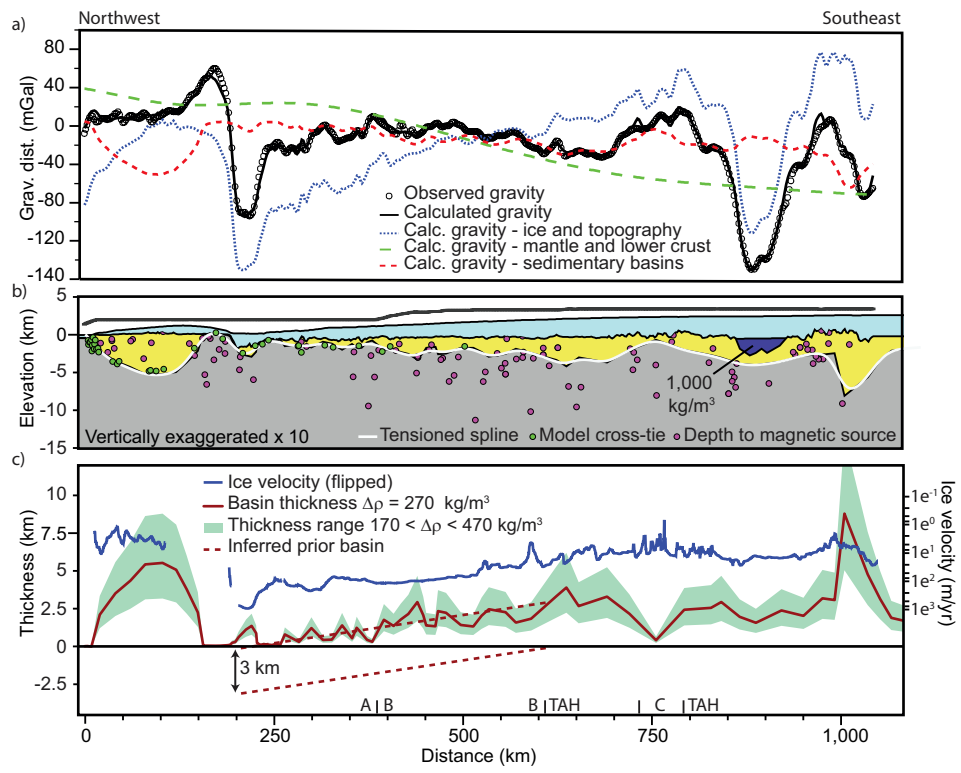
**Extended Data Figure 2 | SSSB base morphology.** The map shows the relationship of the SSSB base morphology with basement faults (dashed black lines), and the locations of the representative model profiles: flight lines Y07b (Extended Data Fig. 3), R03Ea (Extended Data Fig. 4), R06Ea

(Fig. 2), R08Eb (Extended Data Fig. 5) and GL0092a (Extended Data Fig. 6). Arrows indicate the right of the associated model figure in each case. The interpreted erosion boundaries are also shown, in grey, with solid, dashed and dotted lines as in Fig. 1.



**Extended Data Figure 3 | Gravity model along flight line Y07b.** **a**, The observed and calculated gravity disturbance, including model components from ice and topography, the deep crust and Moho ('mantle and lower crust'), and the sedimentary basins. **b**, The model, also showing estimates of depth to magnetic basement, the tensioned spline fit, and cross-ties with other models. Ice, sedimentary rock and basement densities are

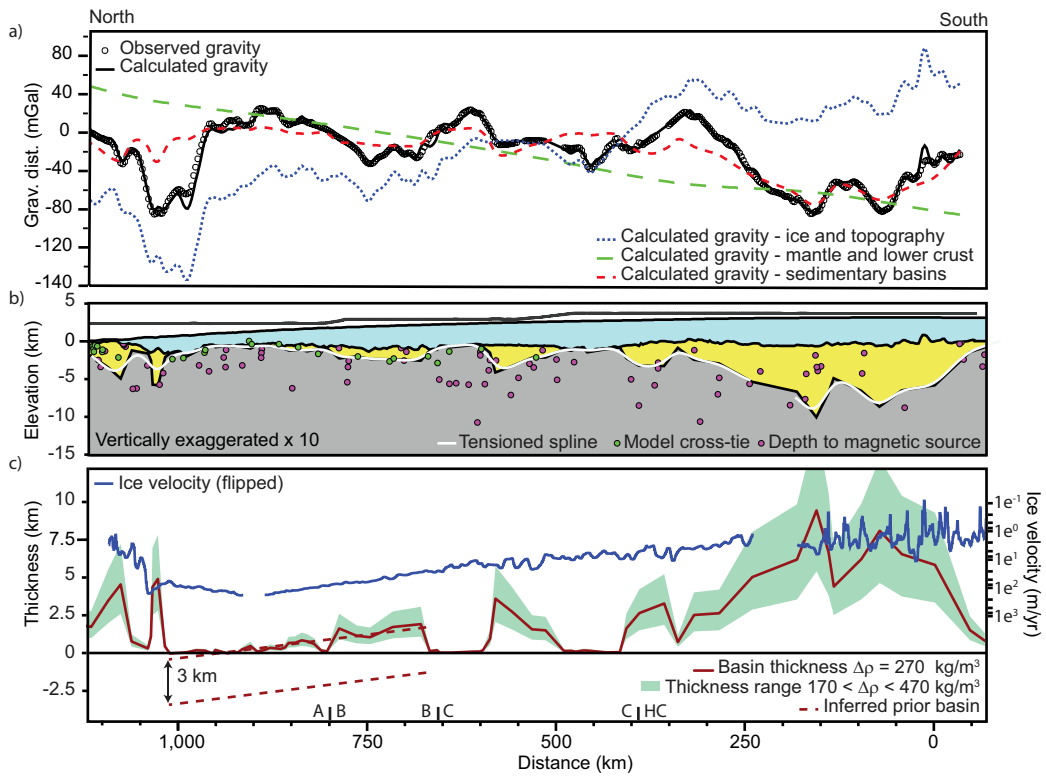
as per Fig. 2. **c**, SSSB thickness and present-day surface ice velocity (vertically flipped). Basin thickness is shown for a density contrast of  $270 \text{ kg m}^{-3}$  ( $2,400 \text{ kg m}^{-3}$ ), and a thickness range for density contrast of  $170\text{--}470 \text{ kg m}^{-3}$  ( $2,200\text{--}2,500 \text{ kg m}^{-3}$ ). Average error in ice-sheet velocity on this line is  $8.4 \text{ m yr}^{-1}$  (ref. 12).



**Extended Data Figure 4 | Gravity model along flight line R03Ea.**

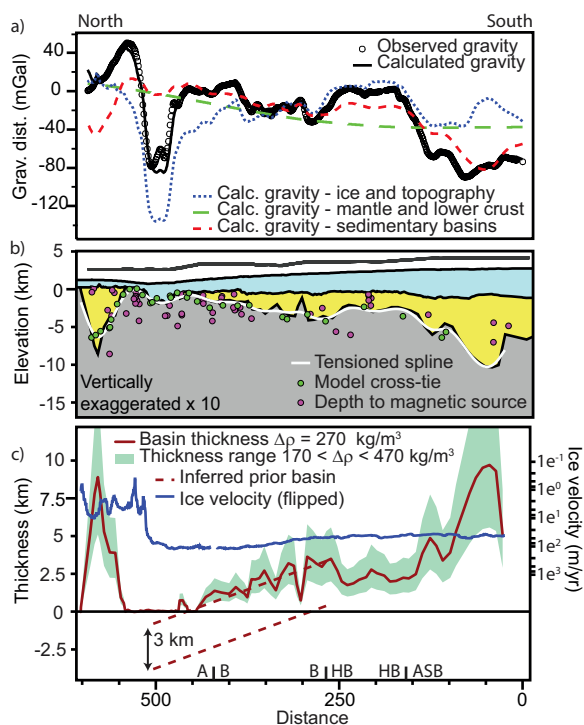
**a,** The observed and calculated gravity disturbance, including model components from ice and topography, the deep crust and Moho ('mantle and lower crust'), and the sedimentary basins. **b,** The model, also showing estimates of depth to magnetic basement, the tensioned spline fit, and cross-ties with other models. Ice, sedimentary rock and basement densities

are as per Fig. 2. **c,** SSSB thickness and present-day surface ice velocity (vertically flipped). Basin thickness is shown for a density contrast of  $270 \text{ kg m}^{-3}$  ( $2,400 \text{ kg m}^{-3}$ ), and a thickness range for density contrast of  $170\text{--}470 \text{ kg m}^{-3}$  ( $2,200\text{--}2,500 \text{ kg m}^{-3}$ ). Average error in ice-sheet velocity on this line is  $9.7 \text{ m yr}^{-1}$  (ref. 12). TAH, Terre Adelie highlands.



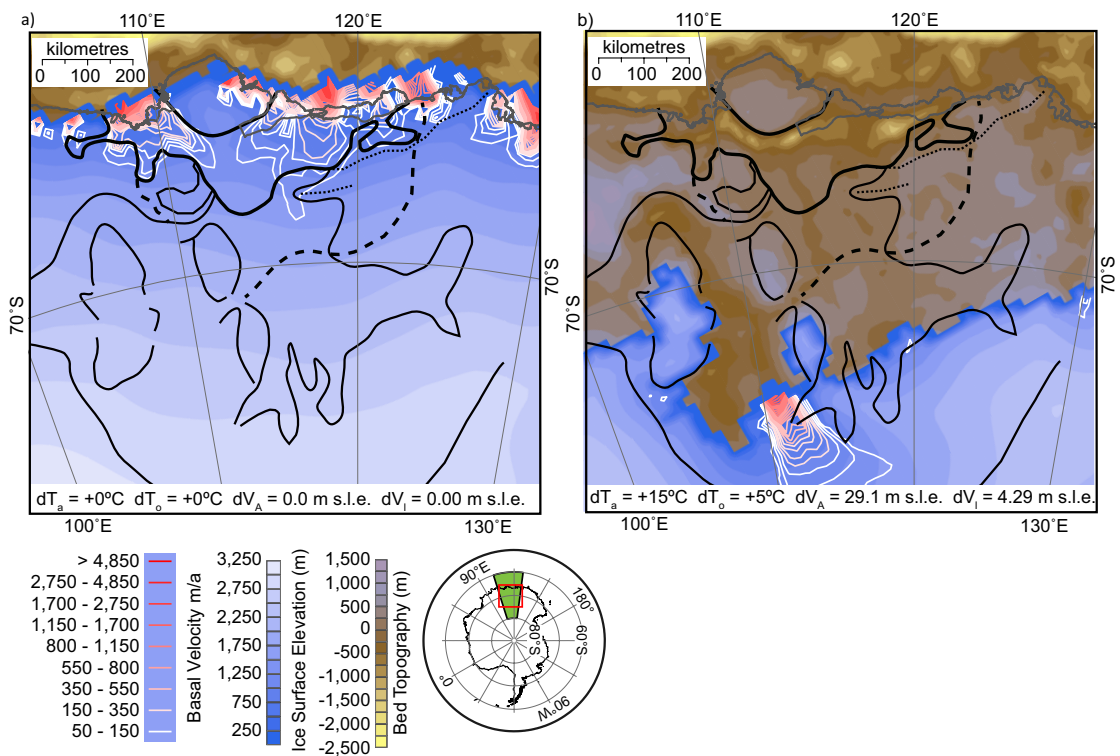
**Extended Data Figure 5 | Gravity model along flight line R08Eb.** **a,** The observed and calculated gravity disturbance, including model components from ice and topography, the deep crust and Moho ('mantle and lower crust'), and the sedimentary basins. **b,** The model, also showing depth to magnetic basement estimates, the tensioned spline fit, and cross-ties with other models. Ice, sedimentary rock and basement densities are as

per Fig. 2. **c,** SSSB thickness and current surface ice velocity (vertically flipped). Basin thickness is shown for a density-contrast of  $270 \text{ kg m}^{-3}$  ( $2,400 \text{ kg m}^{-3}$ ), and the thickness range for density contrast of 170 to  $470 \text{ kg m}^{-3}$  ( $2,200$  to  $2,500 \text{ kg m}^{-3}$ ). Average error in ice-sheet velocity on this line is  $8.6 \text{ m yr}^{-1}$  (ref. 12). HC, Highland C.



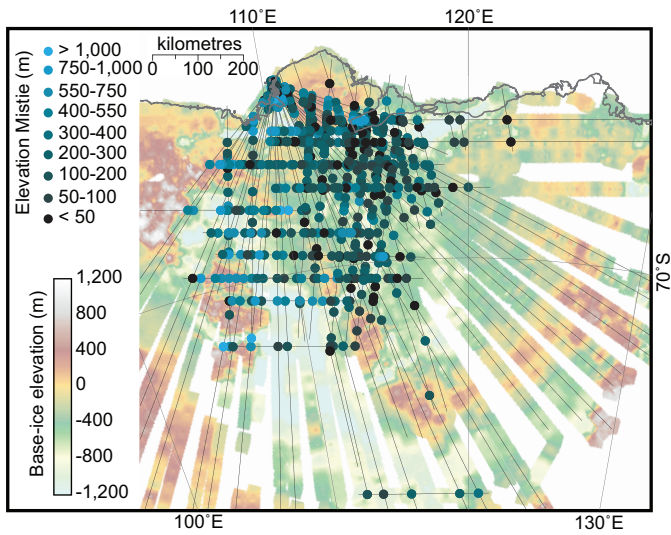
#### Extended Data Figure 6 | Gravity model along flight line GL0092a.

**a**, The observed and calculated gravity disturbance, including model components from ice and topography, the deep crust and Moho ('mantle and lower crust'), and the sedimentary basins. **b**, The model, also showing estimates of depth to magnetic basement, the tensioned spline fit, and cross-ties with other models. Ice, sedimentary rock and basement densities are as per Fig. 2. **c**, SSSB thickness and present-day surface ice velocity (vertically flipped). Basin thickness is shown for a density contrast of  $270 \text{ kg m}^{-3}$  ( $2,400 \text{ kg m}^{-3}$ ), and a thickness range for density contrast of  $170\text{--}470 \text{ kg m}^{-3}$  ( $2,200\text{--}2,500 \text{ kg m}^{-3}$ ). Average error in ice-sheet velocity on this line is  $10.6 \text{ m yr}^{-1}$  (ref. 12). HB, Highland B; ASB, Aurora Subglacial Basin.

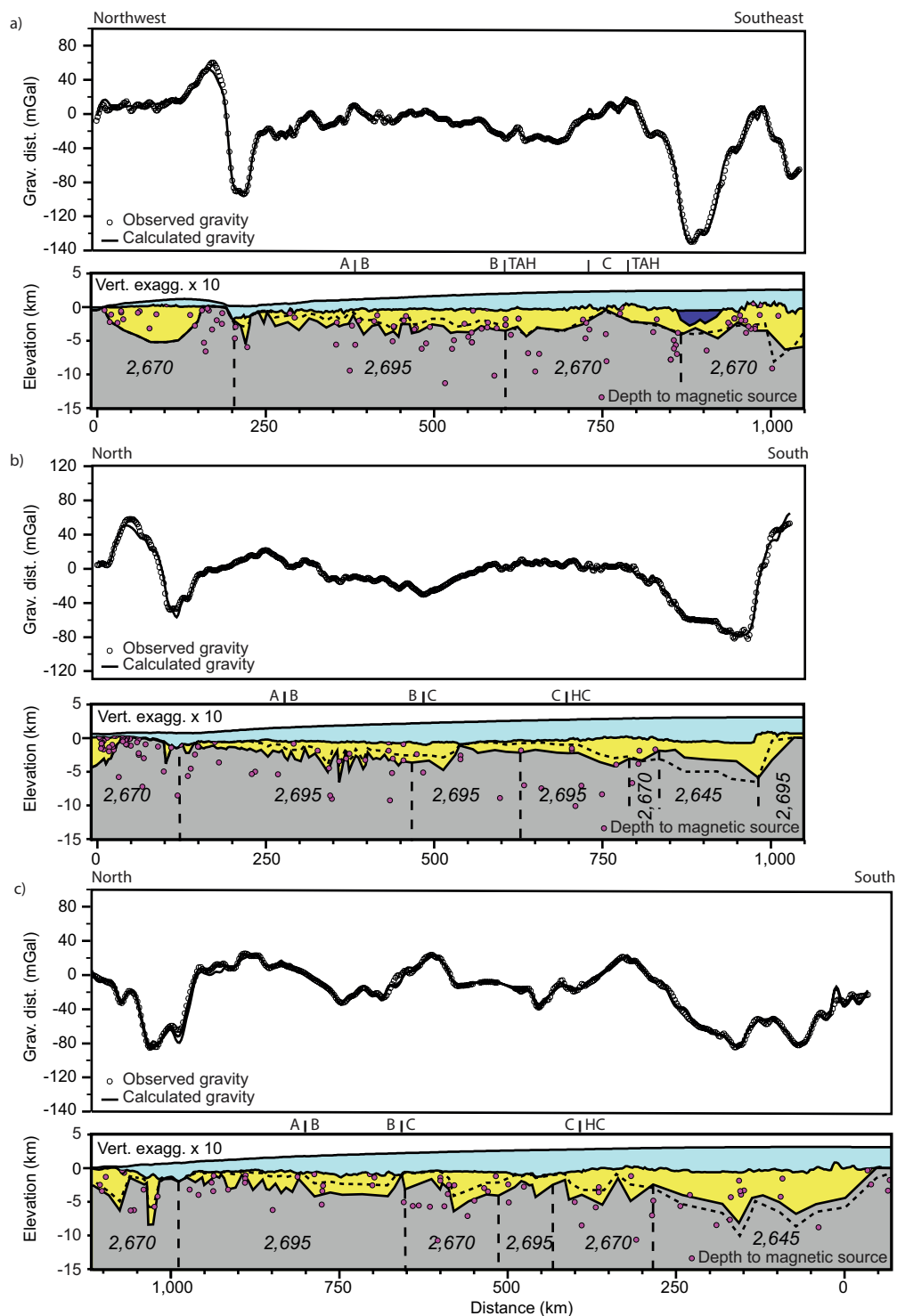


**Extended Data Figure 7 | Additional ice-sheet models.** Ice-sheet surface and bed elevations and basal velocity contours are shown after a long-term, 20-kyr run under constant climate forcing. **a**, With air and ocean temperatures identical to today's ( $dT_a = 0^\circ\text{C}$  and  $dT_o = 0^\circ\text{C}$ ), the ice-sheet margin is located near its present location, and high basal velocities are focused in region A. This model includes ice shelves, which

also have high basal velocity. **b**, With  $dT_a = +15^\circ\text{C}$  and  $dT_o = +5^\circ\text{C}$ , the ice-sheet margin has retreated deep into the ASB and is preserved mainly on inland highlands. Sea-level contributions are defined for all Antarctica ( $dV_A$ ) and for the ASB/SSB sector ( $dV_I$ ), denoted by the green region in the inset.



**Extended Data Figure 8 | Model intersection misfits for the gravity models.** The dots show the value in metres of each tensioned spline mis-tie after model levelling was applied. Levelling applied a constant value to the base of the sedimentary basin on each line to achieve an optimal minimum-norm fit to all cross-ties. Rugged subglacial topography (background) is the main source of non-systematic model errors because of three-dimensional effects.



**Extended Data Figure 9 | Gravity models including basement density variations.** a, Line R03Ea; b, line R06Ea; c, line R08Eb. Each top panel shows the observed and calculated gravity disturbances. Each bottom panel shows the revised model incorporating basement density contrasts between major crustal blocks. The vertical long-dashed lines indicate the major faults. The dotted line indicates the basin structure with a homogeneous basement density of  $2,670 \text{ kg m}^{-3}$ , as shown in previous figures. Fault locations are derived from the interpretation shown

in Extended Data Fig. 1. The fault dip was not tested, as it is a minor component of the field. Blocks are changed by  $\pm 25 \text{ kg m}^{-3}$  in accordance with models of the comparable region in Australia. Italized numbers indicate the basement block densities that generated the flattest basin base. Thickness differences are substantial in places, but the overall pattern of basin thickness is preserved. A/B, B/C and so on indicate the interpreted erosional regions as defined in previous figures.



Extended Data Table 1 | Zonal characteristics of topography and sedimentary rock thickness

Region	Subglacial topography	Sedimentary rock thickness	Bed roughness and basal reflectivity <sup>13</sup>
SSB region A	Deep troughs, reaching -2400m elevation associated with major glaciers (Totten, Moscow University, Vanderford). Hinterland region of generally elevated (ca. -200m) terrain, with a hilly to lineated texture, cut by several channels with up to 600m relief. These channels are aligned with present-day ice flux.	Zero to ~ 1 km, Thinnest at the head of Totten Glacier Thickens towards South-east Thick beneath floating ice shelves	Moderate to high bed roughness High basal reflectivity
SSB region B1	Lower elevation region (ca. -500 m) cut by two ~40 km wide major channels. The main region has a smooth texture. Western channel leads to the ASB via Highland B, and deepens inland from -800m to -1000m in elevation. Eastern channel at ca. -800m elevation leads to region C. This channel possesses several branches leading to the east	Ca. 2-3 km in centre of the zone. Less where channels present, ca. 1-1.5 km, and significantly thinner at zones of confluence (<500m)	Moderate to low bed roughness Low basal reflectivity
SSB region B2	More elevated regions (-400 m to 0m), sloping towards the centre of the SSB. Moderately hilly texture with no major channels.	Ca 1.5-2 km in northwest, 2.5 -3 km in southeast >4 km beneath Highland B	Moderate to high bed roughness, especially at short wavelengths Moderate basal reflectivity
SSB region C	Moderate to very low elevation (0 to -1200 m). Strongly sloping towards the centre of region C. Several branches lead up to Highland C and Terre Adelie highlands, with an overall dendritic pattern.	Typically <500 m. with patchy thicker areas (1-2 km) between channels. One large 3km thick area located between channels at boundary with region B1.	Moderate to high bed roughness Low basal reflectivity
ASB	Very low elevation (-1000 to -1500 m). Smooth texture. Central ridge (-700 to 0 m) separates two deep channels.	Very thick (> 5 km) except in north (2-3 km), and generally thickens to the south	Very low bed roughness High basal reflectivity
VSB	Low elevation (-400 to -800 m), fairly smooth texture. No major channels.	Thick (3-6 km) and generally thickens to the southwest	Low to very low bed roughness High basal reflectivity
Highland Regions	Elevated (>-100m elevation) and typically rough textures. Cut by channels and fjords near ASB.	Low or zero thickness on Ridge B, Dome C, Knox Coast. Moderate to thick thickness on Highlands A, B, C, Law Dome and Terre Adelie Highlands	Typically high bed roughness Typically low basal reflectivity

The listed variations in the characteristics of subglacial topography and the preserved thickness of sedimentary rocks were used to define the zones identified in Fig. 1. The table also documents basal roughness and basal reflectivity characteristics from prior studies<sup>13</sup>, although these were not used to guide our interpretation.